

Numerical Simulation of Propeller-Rudder Interaction for Non-Cavitating and Cavitating Flows Using Different Approaches

S. Berger, M. Scharf, U. Götttsche, J. C. Neitzel, R. Angerbauer, M. Abdel-Maksoud

Institute for Fluid Dynamics and Ship Theory, Hamburg University of Technology, Hamburg, Germany (www.panmare.de)

ABSTRACT

The present article deals with the numerical investigation of propeller-rudder interaction. The involved simulation method is based on coupling a RANS solver and a potential-theory based panel method, where the panel method primarily handles the propeller flow and the RANS solver is used for the simulation of the complex rudder flow. Compared to full RANS simulations, this separation allows numerical investigations in a time-saving manner. In a numerical study, a rudder-propeller combination is evaluated by means of the developed simulation method for different propeller advance coefficients and rudder angles. Rudder cavitation is also addressed. The results are compared to results obtained by a full RANS simulation.

Keywords

Propeller-rudder interaction, viscous/inviscid coupling, rudder performance, rudder cavitation

1 INTRODUCTION

The purpose of marine rudders is to enable the ship to maintain or change its course. Apart from obvious design criteria like the ability to produce sufficient side forces, a well-designed rudder generates low drag forces, is only little susceptible to cavitation and covers a wide range of rudder angles without getting into stall. Numerical methods are able to simulate the hydrodynamic behaviour of rudders and offer the possibility of improving the design.

In a propeller-rudder combination, hydrodynamical interaction effects take place, making both components behave in a different way than they would behave without the presence of the other component. Thus, when analysing the hydrodynamic performance of a rudder, it is essential to also include the propeller in the investigations.

The most important effects of hydrodynamical interaction are outlined in the following. A comprehensive explanation can be found in (Weicker 1965). It is assumed that the interaction effects can be classified according to the direction in which they act. This is one of the assumptions the simulation method presented in this paper is based on.

Propeller → *rudder*. Primarily, the influences of the propeller flow on the rudder are:

- (A1) The rudder is exposed to the vortical slipstream of the propeller, which obviously has an effect on the rudder forces. The slipstream is disturbed by the rudder and consequently the rudder forces differ from

the only theoretically possible situation where the slipstream is unaffected by the presence of the rudder.

- (A2) Furthermore, finite thickness and chord length of the propeller blades induce a displacement flow.

Rudder → *propeller*. There are two major mechanisms present in how the rudder affects the performance of the propeller:

- (B1) Due to its finite thickness and chordlength, the rudder blocks the flow in the vicinity of the propeller. The rudder lift generates an additional velocity disturbance in the propeller plane and in front of the propeller.

- (B2) Apart from this, the aforementioned disturbance of the propeller slipstream, which mainly appears as reduction of the slipstream twist, changes the forces acting on the propeller.

The strength of the interaction effects depends predominantly on the distance between propeller and rudder and on the propeller load. Since the velocity field induced by the propeller depends on the angular position of the propeller blades, the flow field is changing in time.

A number of experimental studies have been devoted to the interaction between rudder and propeller and numerical investigation of this phenomenon has been a research issue for some decades. A review of these activities can be found in (Molland and Turnock 2007). In order to numerically investigate a rudder operating behind a propeller, the simulation method should be able to cover all relevant propeller-rudder interaction effects. RANS methods do this inherently, and – despite computational costs – nowadays their application to simulation of flows is a technical standard in the maritime industry.

Potential-theory based methods allow simulations within an affordable time frame; however, some difficulties arise when they are used for the simulation of propeller-rudder combinations. Being the rudder inflow velocity, the rotational propeller slipstream violates the basic potential theory assumption of irrotational flow (Söding 1999). Despite this deficit, satisfactory results can be obtained by potential-theory based methods. Treating the considerable cross flow along the trailing edge and the numerical problems that occur when surface discretization elements repre-

senting the slipstream interact with the rudder remain challenges in the potential-theory methods, see e.g. (Li 1996), (Han et al. 2001) or (Felli et al. 2006).

In this paper, an alternative approach is applied which basically consists of coupling a RANS method with a potential-theory based method. This viscous/inviscid coupling already has been used with some modifications in earlier works for the simulation of rudders working behind a propeller, for instance see (Moctar 2001), (Natarajan 2003) or (Laurens 2003). All these works have in common that in the viscous flow region treated by the RANS method the geometrically resolved propeller is replaced by a corresponding distribution of body forces calculated by a potential-theory based method. Using this approach can significantly decrease computational effort and time. In (Berger et al. 2013) a simulation tool based on coupling a RANS solver and a panel method has been used for the prediction of pressure fluctuations on the ship hull induced by the propeller; other applications are reported in (Greve et al. 2012). In this work, the tool is enhanced in order to better capture propeller-rudder interaction, including cavitation effects occurring on the rudder.

The paper is organised as follows: After a brief description of the underlying methods in Sections 2.1 and 2.2, the bodyforce coupling algorithm is outlined in Section 2.3 and the overall simulation process is explained in the subsequent section. Section 4 reports on a numerical study in which a propeller-rudder combination has been investigated by the present simulation method and the results are compared to those obtained by a fully viscous simulation and available experimental data provided by SVA Potsdam.

2 CALCULATION METHOD

The basic idea behind the calculation method used in this work is to split the flow problem into two interacting parts, each one covering different flow details, see Figure 1. The viscous flow domain Λ covers flow effects which are strongly influenced by viscosity, i.e. the wake flow around the ship hull (in case of a ship being part of the investigations), as well as complex flow phenomena like the vortical propeller slipstream interacting with the rudder or cavitation forming on complex rudder forms.

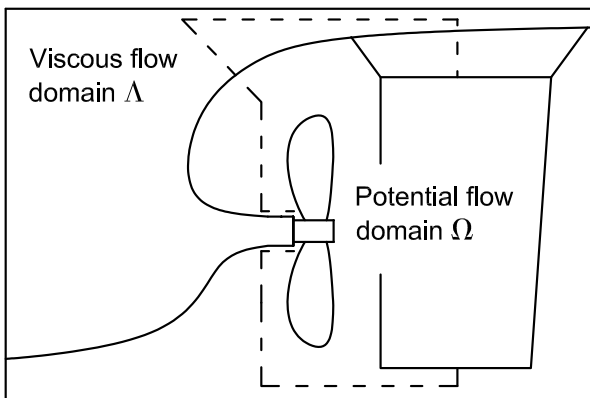


Figure 1: Decomposition of the flow.

The potential flow domain Ω treats flow phenomena of po-

tential flow character – the flow directly around the propeller and the blockage effect of the rudder. This division of the flow problem enables combining a RANS solver with a panel method and carrying out simulations in a time-saving manner without losing to much accuracy compared to full RANS simulations. Most of the computational time can be saved by replacing the geometrically resolved propeller in the viscous flow domain by a corresponding distribution of body forces which is derived by the panel method.

In the following subsections, the theoretical background of the underlying methods is summarised briefly and the body force coupling algorithm, which maps the pressure distribution on the propeller blades in the potential flow domain to body forces acting in the viscous flow domain, is outlined.

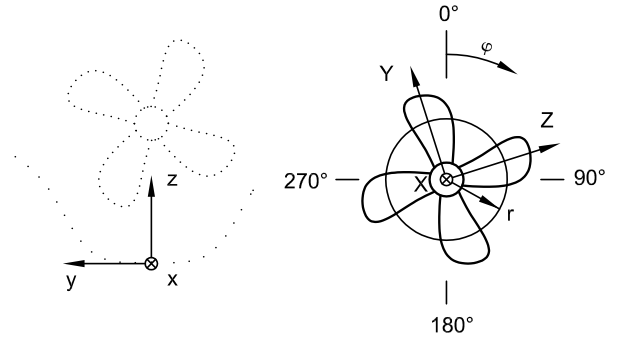


Figure 2: Global (left) and propeller-fixed (right) coordinate system, view from behind.

Figure 2 shows the coordinate systems used throughout the paper. The global coordinate system is fixed to the ship with $\mathbf{x} = (x, y, z)$. However, some of the mathematical formulations are given in a body-fixed coordinate system $\mathbf{X} = (X, Y, Z)$ rotating with the propeller.

2.1 Potential Flow Domain

The flow in the potential flow domain Ω is treated by a low-order panel method. In this work, the in-house code *panMARE* is applied (Bauer and Abdel-Maksoud 2012). A detailed description of the underlying theory is given by Katz and Plotkin (2001).

It is assumed that the total velocity field $\mathbf{U} = \mathbf{U}(\mathbf{x}, t)$ can be divided into a velocity field of the background flow $\mathbf{U}_\infty = \mathbf{U}_\infty(y, z, t)$ which is constant for all x and an induced flow field $\mathbf{U}^+ = \mathbf{U}^+(\mathbf{x}, t)$:

$$\mathbf{U} = \mathbf{U}_\infty + \mathbf{U}^+. \quad (1)$$

Initially, it is assumed that Ω contains only one body, say the propeller. In the *body-fixed* coordinate system (see Figure 2), Equation (1) is rewritten to

$$\mathbf{V} = \mathbf{V}_0 + \mathbf{V}^+ \quad (2)$$

with the total velocity field $\mathbf{V} = \mathbf{V}(\mathbf{X}, t)$ and $\mathbf{V}_0 = \mathbf{V}_\infty + \mathbf{V}_{\text{mot}}$, where \mathbf{V}_∞ is the background flow in propeller-fixed coordinates and \mathbf{V}_{mot} is the velocity component due to the motion of the propeller. The induced flow field \mathbf{V}^+ is considered to be incompressible and irrotational. Hence, a velocity potential $\Phi = \Phi(\mathbf{X}, t)$ with $\mathbf{V}^+ = \nabla\Phi$ and

$\nabla = (\partial/\partial x, \partial/\partial y, \partial/\partial z)$ can be introduced, and the governing flow equations simplify to Laplace's equation for the potential Φ and Bernoulli's equation for the pressure p :

$$\nabla^2 \Phi = 0 \quad (3)$$

and

$$p + \frac{1}{2} \rho |\mathbf{V}|^2 + \rho \frac{\partial \Phi}{\partial t} + \rho g z = p_{\text{ref}} + \frac{1}{2} \rho |\mathbf{V}_0|^2, \quad (4)$$

$\forall \mathbf{X} \in \Omega$ with p_{ref} being a suitable reference pressure. For a lifting body, the boundary $S = \partial\Omega$ is divided into the surface of the body S_B , the surface S_W representing the trailing wake propagating from the trailing edge of the body and the surface S_∞ at infinity. For an arbitrary point $\mathbf{X}_0 \in \Omega$, the potential Φ resulting from a distribution of sources $\sigma = \sigma(\mathbf{X})$ and dipoles $\mu = \mu(\mathbf{X})$ on S_B and dipoles on S_W can be obtained by Green's third identity:

$$\Phi(\mathbf{X}_0) = \frac{1}{4\pi} \int_{S_B \cup S_W} \mu \nabla \left(\frac{1}{d} \right) \cdot \mathbf{n} dS - \frac{1}{4\pi} \int_{S_B} \frac{\sigma}{d} dS, \quad (5)$$

where $\mathbf{n} = \mathbf{n}(\mathbf{X})$ is the normal vector of the surface element dS and $d = \|\mathbf{X} - \mathbf{X}_0\|$. For $\mathbf{X} \in S_B \cup S_W$ holds

$$\sigma = -\nabla \Phi \cdot \mathbf{n} \quad \text{and} \quad \mu = -\Phi. \quad (6)$$

In order to obtain a physically meaningful potential and velocity field, boundary conditions have to be fulfilled on S_B , S_W and S_∞ :

- (1) With growing distance to the body, the influence of the induced velocities must decrease and finally vanish:

$$\mathbf{V}^+ = \nabla \Phi = 0, \quad \forall \mathbf{X} \in S_\infty. \quad (7)$$

The general solution given by Equation (5) fulfills this condition inherently.

- (2) On the surface S_B of the solid body, the impermeability condition is applied, stating that no flow is allowed to penetrate S_B :

$$\mathbf{V} \cdot \mathbf{n} = (\mathbf{V}_0 + \nabla \Phi) \cdot \mathbf{n} = 0, \quad \forall \mathbf{X} \in S_B. \quad (8)$$

- (3) On the wake surface S_W , the Kutta condition is applied to model the vorticity:

$$\Delta p = 0, \quad \forall \mathbf{X} \in S_W, \quad (9)$$

where $\Delta p = p^+ - p^-$ is the pressure jump between the pressure value on the upper and lower side of the trailing wake. Fulfilling the physical Kutta condition (9) in a direct way requires an iterative solution procedure. In order to simplify the calculations, Morino's Kutta condition is applied:

$$\mu_W = \mu_u - \mu_l, \quad (10)$$

defining the relation between the dipole strengths of the upper and lower side of the trailing edge and the dipole strength of the wake surface directly behind the trailing edge. This linearisation holds if the flow direction is perpendicular to the trailing edge.

Equation (5), combined with the above boundary conditions, results in a boundary value problem that is solved by the panel method. Hereby, the surfaces S_B and S_W are discretised by quadrilateral elements and the boundary conditions are applied at the collocation points \mathbf{X}_0 of each panel element. Dipoles and sources are assumed to be constant over one panel. In order to account for the wake roll-up, the wake surface S_W has to be aligned along the streamlines of the velocity field \mathbf{V} in an iterative manner. This, however, entails a huge computational effort, especially if the discretisation of the wake surface is fine. Alternatively, the shape of the surface S_W can be prescribed and considered to be indeformable during the simulation.

For a non-lifting body, modelling the wake flow is omitted. The discretised problem results in a set of linear equations for the unknown source and dipole strengths, which can be solved numerically by the Gauss method.

In a multi-body simulation, the influences of other bodies q have to be taken into account. Considering a particular body, the influences of other bodies can be captured by the velocities $\mathbf{U}_q^+ = \nabla \Phi_q$ induced by body q at the location of the body considered. The background velocity introduced in Equation (1) is then replaced by:

$$\mathbf{U}_\infty^\oplus = \mathbf{U}_\infty + \sum_q \nabla \Phi_q, \quad (11)$$

with $\mathbf{U}_\infty^\oplus = \mathbf{U}_\infty^\oplus(\mathbf{x}, t)$ and $\nabla = (\partial/\partial x, \partial/\partial y, \partial/\partial z)$. The procedure described in this subsection has to be carried out sequentially for all bodies located in the potential flow domain under consideration of the respective corrected background flow \mathbf{U}_∞^\oplus .

2.2 Viscous Flow Domain

For the calculation of the viscous flow in the domain Λ including cavitation effects on the rudder, a commercial RANS code is applied (ANSYS 2014). The cavitating flow is regarded as two phase flow and a mixture model is applied to approximate cavitation effects. The model assumes the fluid to be a mixture of liquid water m and vapour v , where the sum of the volume fractions must be equal to one:

$$\alpha_m + \alpha_v = 1. \quad (12)$$

The density of the mixture ρ^* is obtained by

$$\rho^* = \alpha_m \rho_m + \alpha_v \rho_v, \quad (13)$$

where ρ_v is the density of vapour and ρ_m the density of liquid water (containing a certain amount of dissolved gases). A corresponding relation holds for other material properties. The governing equations describing the behaviour of the flow are the continuity equation

$$\frac{\partial \rho^*}{\partial t} + \nabla \cdot (\rho^* \mathbf{u}) = 0 \quad (14)$$

and the momentum equation

$$\left(\frac{\partial}{\partial t} + \mathbf{u} \cdot \nabla \right) (\rho^* \mathbf{u}) = -\nabla p + \nabla \cdot (\boldsymbol{\tau} + \boldsymbol{\tau}_T) + \mathbf{f}, \quad (15)$$

$\forall \mathbf{x} \in \Lambda$. In Equation (15), the variable \mathbf{u} denotes the Reynolds-averaged velocity, p the Reynolds-averaged pressure, $\boldsymbol{\tau}$ the Reynolds-averaged molecular stress tensor and $\boldsymbol{\tau}_T$ the Reynolds stress tensor due to the Reynolds-averaging, whose components are approximated by appropriate turbulence models. \mathbf{f} is a volume specific force source term. This term will become important later in Section 2.3.

Transport and production of both phases are described by the volume-fraction equation

$$\frac{\partial}{\partial t} (\alpha_m \rho_m) + \nabla \cdot (\alpha_m \rho_m \mathbf{u}) = \dot{S}_l, \quad (16)$$

$\forall \mathbf{x} \in \Lambda$, where the source term \dot{S}_l of the liquid phase is simply related by $\dot{S}_l = -\dot{S}_v$ to the source term of the vaporous phase \dot{S}_v . The volume fraction of the vaporous phase results from Equation (13). Determining the source term \dot{S}_v is the task of the particular cavitation model. In this case, the cavitation model described and developed by Bakir et al. (2004) is used. Apart from some material and empirical constants, the source term is proportional to

$$\dot{S}_l \sim -F_c \sqrt{|p_v - p|} \operatorname{sgn}(p_v - p) \quad (17)$$

with p_v being the vapour pressure of water, $F_c = 50$ for $p_v - p > 0$ and $F_c = 0.01$ for $p_v - p < 0$ taking into account that vaporisation happens much faster than condensation. The relation in Equation (17) originates from the idea that a volume unit contains a number of vapour bubbles whose growing and shrinking behaviour is modelled by means of the Rayleigh-Plesset equation. In order to simplify the model, the higher-order terms of this equation are truncated.

In case of non-cavitating flow, the density ρ^* becomes a constant $\rho^* = \rho$, Equation (16) is redundant and all time derivatives of the density vanish in Equations (14) and (15).

For the numerical solution of the above equations under consideration of appropriate boundary and initial conditions, the ANSYS CFX code based on a finite volume element method which can be applied for both structured and unstructured numerical grids is used.

2.3 Body Force Coupling Algorithm

One basic idea of the simulation tool developed in this paper is to replace the geometrically resolved propeller in the viscous flow domain Λ by a corresponding distribution of body forces transferred from the potential flow domain Ω . The mapping algorithm involved is able to convert the pressure distribution on the blades to volume-specific body forces and has been implemented in ANSYS CFX user coding. It can handle both structured and unstructured meshes and takes into account the propeller shape including pressure and suction side of the blades. From now on, the notation of the theory in a continuous form will be abandoned and a discretised form will be used instead.

For each time step, the panel method provides the center \mathbf{x}_k and the four vertices $\mathbf{x}_{c,l,k}$, $l = 1, \dots, 4$ of each panel k . The area A_k , pressure p_k and the normal vector \mathbf{n}_k yield

the force $\mathbf{F}_k = p_k A_k \mathbf{n}_k + \mathbf{F}_{\text{fr},k}$ acting on the panel. $\mathbf{F}_{\text{fr},k}$ is an empirically estimated friction force.

$\Lambda_P \subset \Lambda$ is defined as the part of the viscous flow domain containing the virtual propeller. The volume mesh consists of a number of control volumes dV_m surrounding the grid vertices \mathbf{x}_m .

First, the mesh in the subdomain Λ_P is analysed and an equivalent cell radius $r_{s,m}$ is assigned to each control volume dV_m :

$$r_{s,m} = \beta \sqrt[3]{dV_m}, \quad (18)$$

where $\beta = 1.0 \dots 2.0$ is a model parameter regulating how sharp the propeller shape is reproduced in the viscous flow domain. Knowing $r_{s,m}$ for each control volume m , it is detected which panels k are intersected by the control volume m . This is done by means of the following definition:

$$a_{k,m} = \begin{cases} 1 & \text{if } \|\mathbf{x}_m - \mathbf{x}_k\| \leq r_{s,m} \\ & \forall \|\mathbf{x}_m - \mathbf{x}_{c,l,k}\| \leq r_{s,m}, l = 1, \dots, 4 \\ 0 & \text{else} \end{cases} \quad (19)$$

Furthermore, the number of panels intersected by the m -th control volume is of concern:

$$b_m = \begin{cases} 1 & \text{if } a_{k,m} = 0 \forall k \\ \sum_k a_{k,m} & \text{else} \end{cases}. \quad (20)$$

The distribution of body forces $\mathbf{f}_{\text{bf},m}$ added to the source term of the momentum Equation (15) is then obtained by

$$\mathbf{f}_{\text{bf},m} = \sum_k \frac{a_{k,m}}{b_m} \frac{\mathbf{F}_k}{V_k} \text{ with } V_k = \sum_m \frac{a_{k,m}}{b_m} dV_m. \quad (21)$$

The coupling algorithm described so far works without any problems for non-cavitating flow. No experience is available concerning whether the algorithm in combination with the cavitation model presented in Section 2.2 is able to handle propeller cavitation in a physically reasonable way. Thus, the numerical studies carried out in this work for cavitating flow are confined to those cases where no or only little cavitation occurs on the propeller blades, and the focus is set on rudder cavitation. However, even in cases without cavitation on the blades, numerical problems related to the impact of body forces arise when the cavitation model is activated. To overcome these problems, the body force distribution obtained by Equation (21) is corrected by the volume fraction $\alpha_{m,m}$ which leads to

$$\mathbf{f}_{\text{bf},m}^* \approx \alpha_{m,m} \mathbf{f}_{\text{bf},m}. \quad (22)$$

3 SIMULATION PROCEDURE

In this section, the overall simulation procedure is depicted. The procedure is shown in Figure 3. Consider the most general case of a propeller-rudder combination working behind a ship. In that case, the viscous flow domain Λ contains the ship hull and the rudder with all relevant details. The subdomain Λ_P serves as retainer for the virtual propeller. The potential flow domain Ω consists essentially of the propeller, the rudder and parts of the hull directly above the propeller. It is not necessary to model the rudder with the same level of detail as in the viscous flow domain,

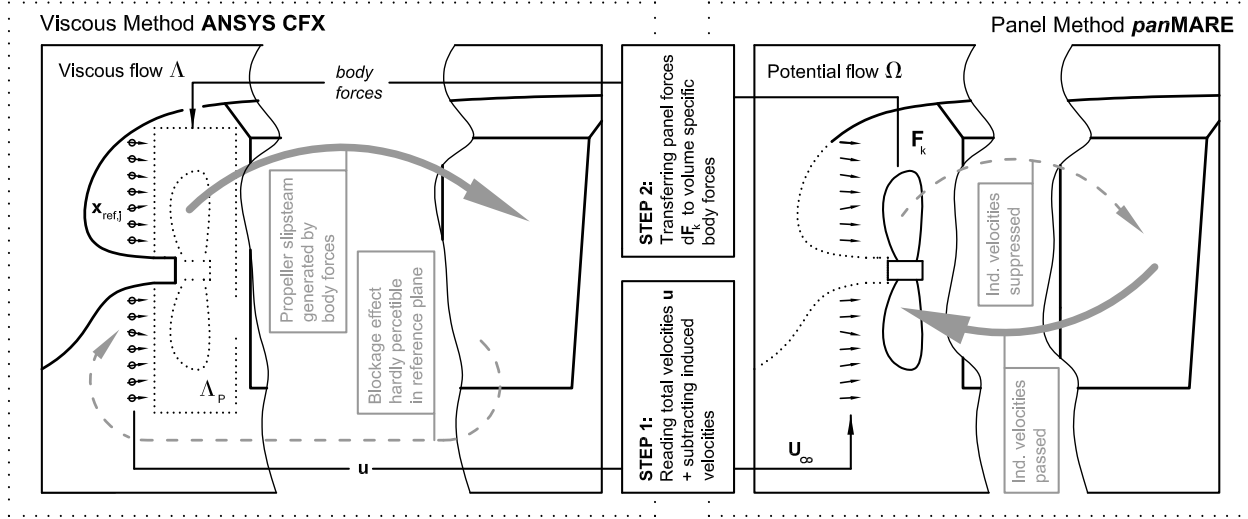


Figure 3: Principle of the simulation method. Interaction effects are denoted by grey arrows.

since complicated flow details, as for example, gap flows or rudder cavitation are not analysed in the potential flow domain. The unsteady simulation procedure consists of two major steps:

Step 1. The velocity distribution \mathbf{u} is extracted from the viscous flow domain for a number of control points $\mathbf{x}_{\text{ref},j}$ (typically 500...600) located in a reference plane upstream the propeller, i.e. $x_{\text{ref},j} = x_{\text{ref}} = \text{const. } 0.25D$ has proven to be an adequate distance between propeller and reference plane (Greve et al. 2012). The velocity in the reference plane is affected by the wake flow of the ship, the suction effect of the (virtual) propeller and the influence of the rudder. Due to the distance between rudder and reference plane, the latter is only perceptible to a minor extent. In order to approximate the effective wake field serving as background flow \mathbf{U}_{∞} in the potential flow domain, the induced velocities of propeller and rudder are subtracted:

$$\mathbf{U}_{\infty}(t_{[i]}) \approx \mathbf{u}(t_{[i-1]}) \Big|_{x=x_{\text{ref}}} - [\mathbf{U}_P^+(t_{[i-1]}) + \mathbf{U}_R^+(t_{[i-1]})] \Big|_{x=x_{\text{ref}}}, \quad (23)$$

for $\mathbf{x}_{\text{ref},j}$. Since no information on the induced velocities is available for the current time step $t_{[i]}$, the results from the previous time step $t_{[i-1]}$ are used. In the potential flow domain Ω , the propeller flow is calculated considering a modified background flow $\mathbf{U}_{\infty}^{\oplus} = \mathbf{U}_{\infty} + \mathbf{U}_R^+$ according to the explanations in Section 2.1. Note that in contrast to Equation (23) \mathbf{U}_R^+ is now evaluated for the propeller location, not for $\mathbf{x}_{\text{ref},j}$.

At this point, two basic simplifications are made now. For the calculation of the propeller flow in the potential flow domain Ω , a prescribed wake model is used (see Section 2.1) and consequently, the deformation of the propeller slipstream is not taken into account. A further simplification is that the flow around the rudder is determined without accounting for the induced velocities of the propeller. Without these simplifications, advanced models would be required to handle the deformation of propeller wake panels in interaction with the rudder and the computational ef-

fort would increase notably.

Step 2. The pressure distribution on the propeller derived by the panel method is transformed to a corresponding distribution of body forces as described in Section 2.3 and passed to the viscous flow domain Λ . In so doing, the presence of a propeller is emulated influencing the flow around the rudder and the hull. Rudder forces, complex gap flows and rudder cavitation can then be analysed.

The two steps are repeated for every time step considering the current propeller blade position. If the ship hull is not included in the simulation, extracting the velocity field \mathbf{u} is no longer required and only the induced velocities of the rudder have to be considered to determine the background flow of the propeller in the potential flow domain.

4 NUMERICAL STUDY

In this section, the methodology and the results of the numerical study are given. Herein, a rudder-propeller combination operating in homogenous inflow under a flat plate is investigated. Generally, the developed tool is able to consider the influence of the ship hull. In the present study, however, no ship hull is included in order to clearly isolate effects of propeller-rudder interaction from other effects.

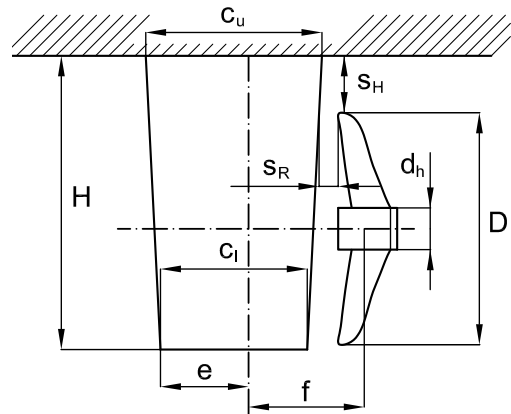


Figure 4: Main dimensions of the investigated propeller-rudder combination.

The main dimensions of the investigated configuration, which is based on the aftship design of the KRISO Container Ship (NMRI 1997), are shown in Figure 4 and Table 1. All simulations are carried out in model scale.

Table 1: Main dimensions and properties of the investigated propeller-rudder combination.

Characteristics		Value	
<i>Propeller KCS</i>			
Type, sense of rot.	1 × FPP, clockwise		
Propeller diameter	$D = 2R$	[m]	0.250
Number of blades	n_b	[-]	5
Hub ratio	d_h/D	[-]	0.180
Area ratio	$A_e/(\frac{\pi}{4}D^2)$	[-]	0.800
Pitch ratio	P/D	[-]	0.996
<i>Rudder</i>			
Type	Untwisted spade rudder		
Profile	NACA0018		
Height	H	[m]	0.313
Chord length	c_u	[m]	0.190
	c_l	[m]	0.158
Lateral area	A_l	[m ²]	0.054
TE – rudder stock	e	[m]	$\frac{3}{5}c_l$
<i>Installation position</i>			
Tip clearance	s_H	[m]	$0.220D$
	s_R	[m]	$0.086D$
Propeller – rudder stock	f	[m]	$0.498D$

The operation conditions chosen for the numerical study are listed in Table 2.

Table 2: Operation points.

Characteristics		Value	
Inflow velocity	V	[m/s]	2.0
<i>Propeller load</i>			
Number of rev.	n	[s ⁻¹]	11.429
	– or –		
	n	[s ⁻¹]	16.0
acc. $J = 0.7$ and $J = 0.5$ with $J = \frac{V}{nD}$			
<i>Rudder load</i>			
Rudder angle	δ	[°]	0
	– or –		
	δ	[°]	10
<i>Cavitation</i>			
non-cavitating flow			
– or –			
Cavitation number	$\sigma_V = \frac{p_{ref} - p_v}{\frac{1}{2}\rho V^2}$	[-]	2.6
	only for $J = 0.7$ and $\delta = 10^\circ$		

The propeller-rudder combination is investigated in two different ways: by means of the simulation tool developed in the present work and by a fully viscous simulation with geometrically resolved propeller. It is assumed that the interaction effects between rudder and propeller are captured correctly by the fully viscous simulation and they are thus appropriate to evaluate the accuracy of the developed viscous/inviscid coupling approach.

4.1 Description of the Numerical Grids

In the following, the grids used for the numerical study are described and some relevant setup parameters are given.

Fully Viscous Simulation Figure 5 illustrates the dimensions of the grid for the fully viscous simulation with ANSYS CFX. The unstructured mesh consists of 4.33 mio. tetrahedra elements whereof 1.65 mio. elements are used to discretise the propeller, 2.31 mio. are arranged in the vicinity of propeller and rudder and 0.37 mio. fill the outer mesh zone.

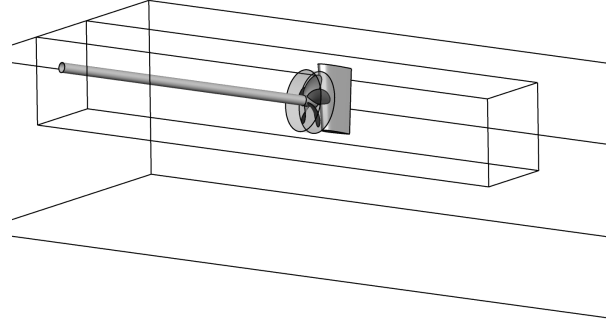


Figure 5: Extent of the numerical grid used for the RANS simulation.

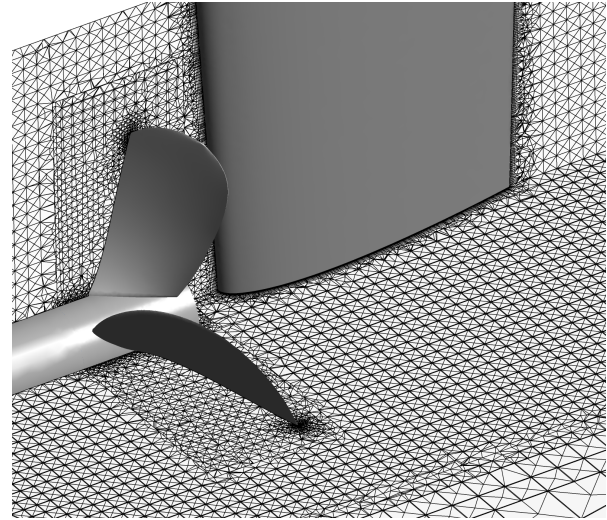


Figure 6: Numerical grid used for the RANS simulation, detail view.

A sliding interface connects the propeller grid and the static part of the grid, see Figure 6. Propeller hub and shaft are modelled as cylinder. The grid resolution around the rudder is relatively fine in order to account for cavitation and boundary layer effects. Since a detailed analysis of the propeller flow is not part of the numerical investigation, the propeller grid is kept coarse. For the simulation of turbulence, the SST turbulence model is employed (ANSYS 2014). The time step size is adjusted in such a way that the angle increment is four degrees.

Coupling Approach In this case, two different grids are necessary: the mesh for the viscous flow domain Λ and

the surface grid discretising the potential flow domain Ω . The former is derived from the mesh mentioned above that is used for the fully viscous simulation by removing the elements which discretise the propeller. This part of the mesh is replaced by empty cells and the sliding interface is no longer needed. Since the mesh density in this zone can be chosen low, almost all elements formerly located in this zone can be saved and the overall number of elements shrinks to 2.69 mio.

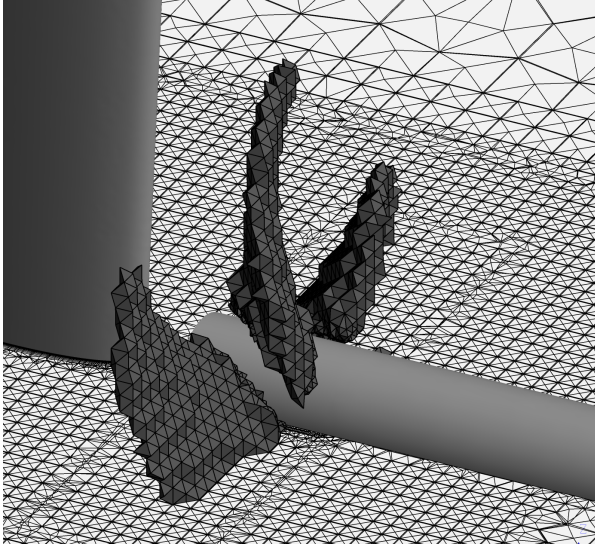


Figure 7: Numerical grid of the viscous flow domain Ω , detail view.

The number of elements representing the virtual propeller in the viscous flow domain depends on the mesh density. In this case, approximately 5700 elements represent the propeller geometry, see Figure 7. The exact number varies slightly with the angular position of the propeller.

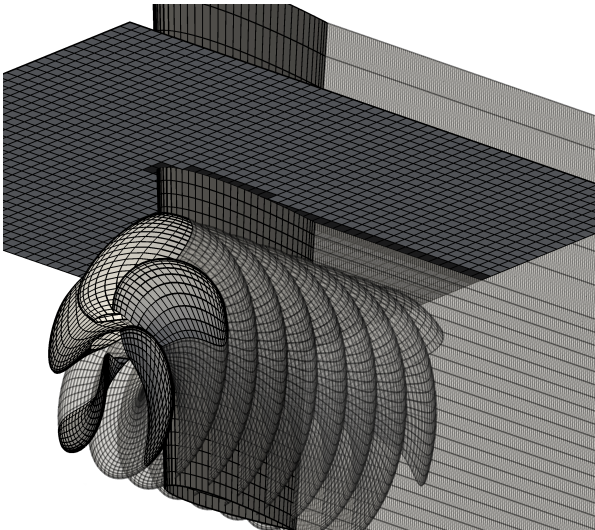


Figure 8: Panel model of the potential flow domain Ω . Deactivated panels on the plate are coloured dark.

Figure 8 shows the surface grid of the potential flow domain consisting of propeller, rudder and a horizontal plate above the propeller. Each propeller blade is discretised by

12 panel elements on pressure and suction side in the circumferential direction and 22 panels in the radial direction with increasing refinement towards the blade tips (528 panels per blade). The propeller hub is not included in the panel model. Capturing the flow around the upper part of the rudder requires a special treatment. In order to keep the model as simple as possible and to avoid complex grid structures in this region, the rudder grid is extended in way that it pierces the plate and those plate panels which are located very close to the rudder are deactivated since they give rise to numerical problems. Similar to the fully viscous simulations, a time step size is chosen which results in an angle increment of four degrees.

4.2 Results

The presentation of the results is organised as follows: First, some integral time-averaged quantities regarding rudder and propeller are given. After this, unsteady flow phenomena are addressed and some relevant results on details of the flow around rudder and propeller are shown. From now on, *RANS* refers to results obtained by the RANS method with geometrically resolved propeller and *CPL* stands for those results obtained by the viscous/inviscid coupling approach developed in this work. Unless explicitly stated, the results presented are related to non-cavitating flow. The discussion of the results will take place in Section 4.3.

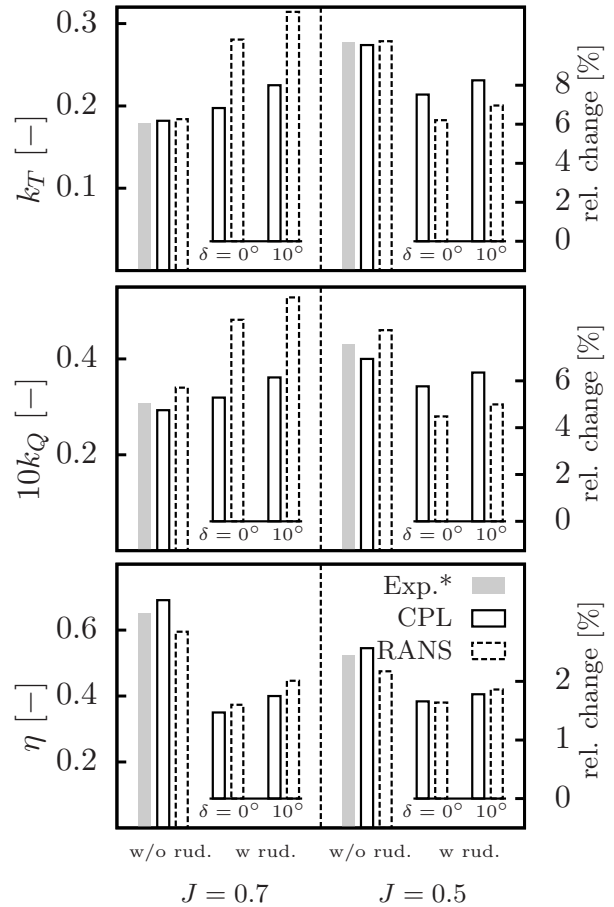


Figure 9: Influence of the rudder on thrust, torque and the efficiency of the propeller for different advance coefficients J and different rudder angles δ .

Integral Time-Averaged Results Figure 9 provides an overview of the predicted time-averaged propeller thrust and torque for different advance coefficients and rudder angles as well as for the case where no rudder influences the propeller flow. Experimental data is only available for open water conditions (Richter and Heinke 2006).

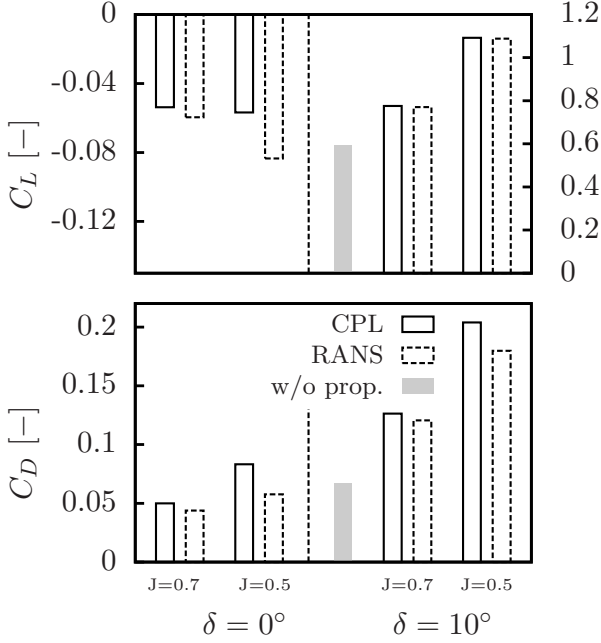


Figure 10: Influence of the propeller on rudder lift and rudder drag for different advance coefficients J and different rudder angles δ .

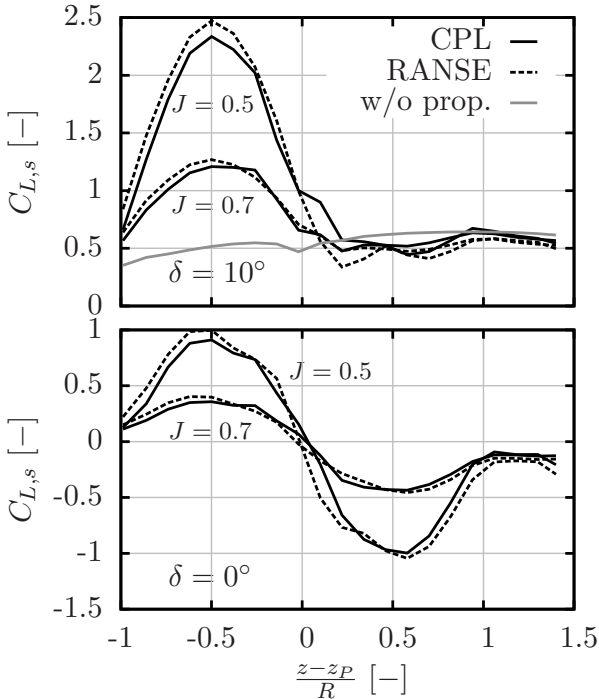


Figure 11: Sectional rudder lift distribution.

The integral forces acting on the rudder are shown in Figure

10 in a dimensionless form:

$$C_L = \frac{\widetilde{F}_y}{1/2\rho A_l V^2} \quad \text{and} \quad C_D = \frac{-\widetilde{F}_x}{1/2\rho A_l V^2},$$

where \widetilde{F}_y and \widetilde{F}_x are the y - and x -component of the time-averaged force acting on the rudder.

A more detailed analysis of the rudder lift is given in Figure 11 in which the sectional lift coefficient

$$C_{L,s} = \frac{d\widetilde{F}_y}{1/2\rho dA_l V^2}$$

is plotted over the relative vertical rudder position $\frac{z-z_P}{R}$ with z_P being the z -coordinate of the propeller axis. For $\delta = 10^\circ$ the lift distribution generated without the presence of the propeller can also be seen in the figure.

Unsteady Flow Phenomena In this section, the focus is put on phenomena which are related to unsteady flow. These include temporal fluctuations of the propeller thrust and fluctuations of the pressure field induced by the propeller. The relative blade thrust fluctuation ϵ_{T_b} is defined here as

$$\epsilon_{T_b} = \frac{T_b - \widetilde{T}_b}{\widetilde{T}_b},$$

where \widetilde{T}_b is the time-averaged blade thrust and T_b is the instantaneous blade thrust. In Figure 12, the fluctuations of the blade thrust for different advance coefficients and rudder angles is shown.

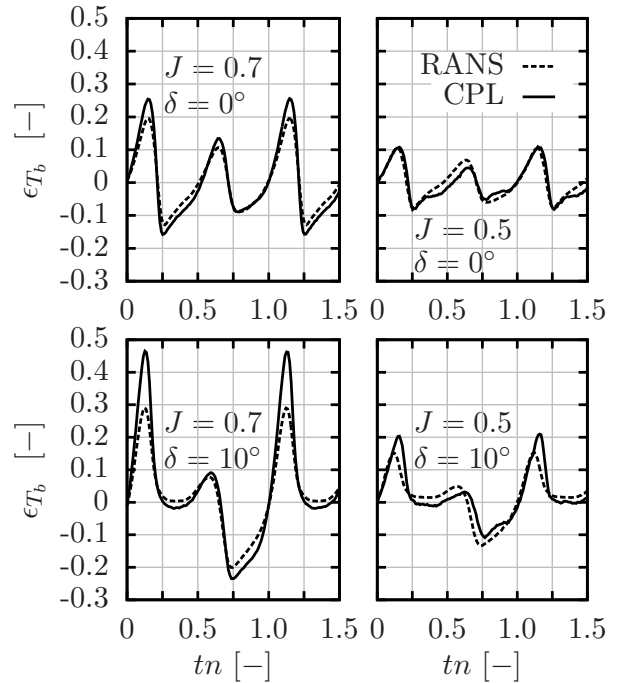


Figure 12: Influence of the rudder on the relative change of blade thrust.

Propeller-induced pressure fluctuations are evaluated by means of a Fourier analysis for a number of monitoring points above the propeller where $x = x_P$, $-0.24 < \frac{y}{R} <$

0.24 and $z = z_H$. x_P denotes the propeller plane and z_H the vertical position of the flat plate or the solid wall above the propeller, respectively. The amplitudes $\hat{p}^{[i]}$ are made dimensionless by

$$k_{p^{[i]}} = \frac{\hat{p}^{[i]}}{\rho n^2 D^2}.$$

The label $[i]$ refers to the frequency inn_b the pressure amplitudes are occurring with. Figure 13 displays pressure fluctuations for $i = 1$ induced by the propeller without and with rudder as well as for different rudder angles. For reasons given later in Section 4.3, pressure fluctuations predicted by means of the coupling approach are observed in the potential flow domain.

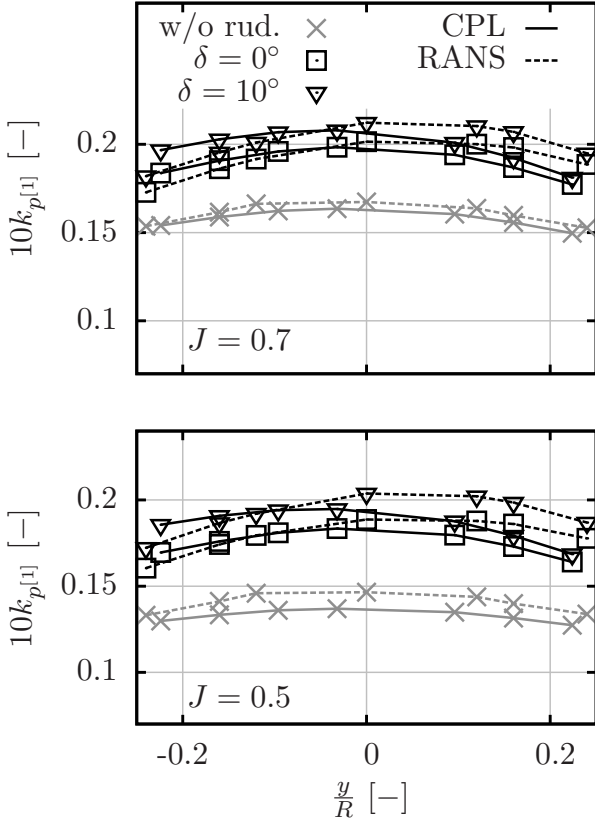


Figure 13: Propeller-induced pressure fluctuations above the propeller.

Selected Flow Details The results presented so far are related to quantities derived from time-averaged or instantaneous surface pressure distributions. In this section, the analysis is extended towards the entire flow field. Figure 14 illustrates the behaviour of the propeller slipstream in interaction with the rudder for $\delta = 0^\circ$ and $J = 0.7$. In the left subfigures, prominent vortex structures propagating from the blade tips are made visible by means of vortex detection criteria available in the ANSYS CFX post processing module for a particular instant of time. On the right hand side, isolines for the axial velocity show the acceleration and the deflection of the flow based on a time-averaged velocity field \tilde{u} .

The coefficients of time-averaged pressure $C_{\tilde{p}}$ and maximum pressure change $C_{\hat{p}}$ are introduced:

$$C_{\tilde{p}} = \frac{\tilde{p} - p_{\text{ref}}}{\frac{1}{2}\rho V^2} \quad \text{and} \quad C_{\hat{p}} = \frac{p_{\text{max}} - p_{\text{min}}}{\frac{1}{2}\rho V^2},$$

with \tilde{p} being the time averaged pressure and p_{max} and p_{min} being the maximum and minimum pressure observed in a particular position, respectively. For $z = z_P - 0.5R$ and in the vicinity of the rudder, $C_{\tilde{p}}$ and $C_{\hat{p}}$ are shown in Figures 15 and 16.

Rudder Cavitation For the analysis of rudder cavitation, the mixture model as described in Section 2.2 is activated. Those zones in the flow where $\alpha_m < 0.5$ are regarded as cavitation. For the reasons given in Section 2.3, rudder cavitation effects are only investigated for $J = 0.7$ where the propeller is only moderately loaded and propeller cavitation is negligible. The considered rudder angle is $\delta = 10^\circ$. The prognosticated cavitation pattern on the rudder for this operation conditions is shown in Figure 17. For a better comparability, reference lines have been drawn in the figure.

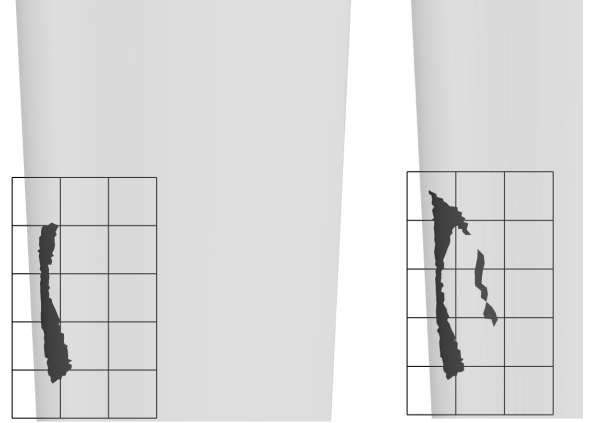


Figure 17: Predicted rudder cavitation for $J = 0.7$ and $\delta = 10^\circ$. The criterion for cavitation used here is $\alpha_m < 0.5$. The topmost line is located at $z = z_P$, the distance between the lines is $0.2R$. Left: CPL, right: RANS.

4.3 Discussion

Recalling the main interaction effects between rudder and propeller mentioned in the introductory Section 1, which of these effects are captured by the simulation tool?

Propeller \rightarrow rudder. The rudder side forces predicted by the simulation tool show good agreement with the RANS simulation results, especially for $\delta = 10^\circ$, see Figure 10. For $\delta = 0^\circ$, some deviations occur. However, predicting the side force of the rudder with zero rudder angle is challenging, because in this case, the relatively small side force is the remainder of two bigger forces acting contrarily on the upper and the lower half of the rudder. Figure 11 illustrates this. The developed simulation tool provides good results with respect to the rudder drag at $J = 0.7$ where the propeller is moderately loaded. The accordance of these integral quantities indicate that the influence the deformed

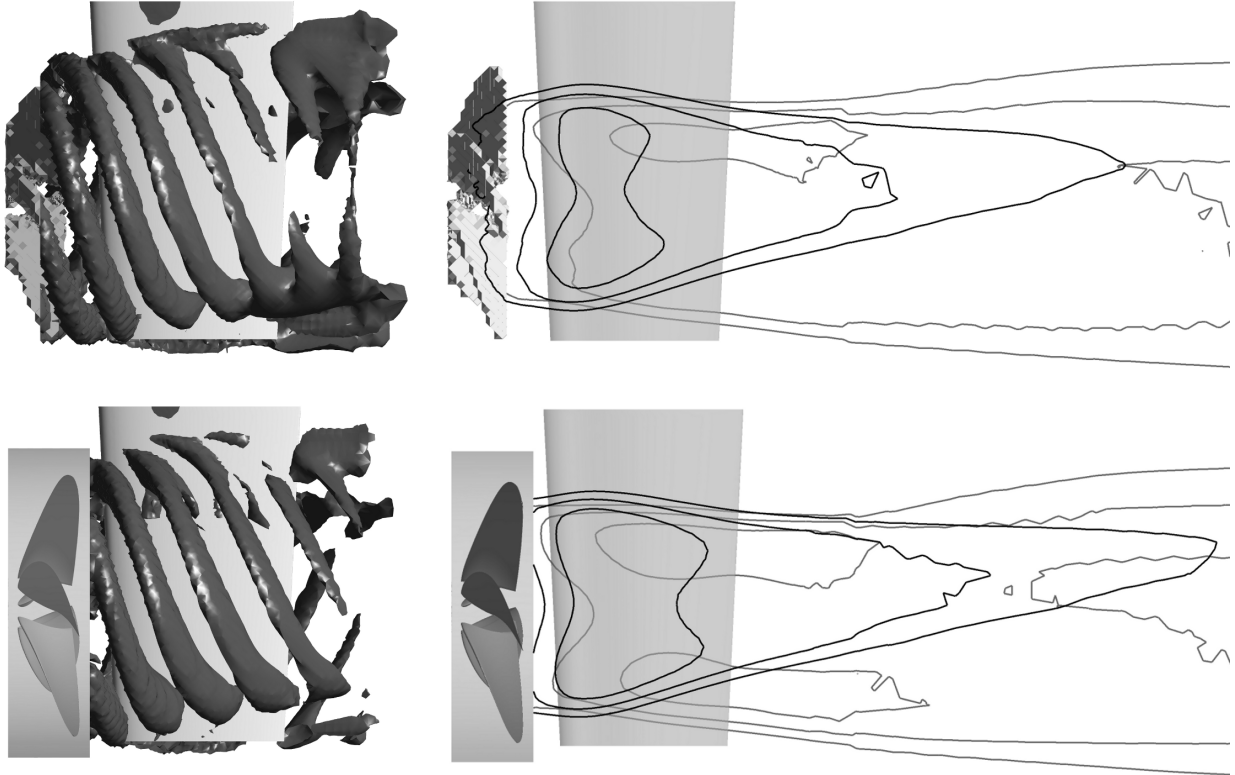


Figure 14: Left: Visualisation of tip vortex structures. Right: Isolines of axial velocity for $1.25 < \frac{u_x}{V} < 1.75$ at $y = 0.5R$ (black) and $y = -0.5R$ (grey). CPL top, RANS bottom; operation conditions: $J = 0.7$ and $\delta = 10^\circ$.

propeller slipstream has upon the rudder (A1, ref. Section 1) is sufficiently captured by the developed approach. This is also a basic condition for a reliable cavitation analysis. The predicted cavitation shapes shown in Figure 17 differ only in detail, especially in the upper region where the propeller hub affects the flow.

No noticeable differences become evident regarding the time-averaged pressure field around rudder and propeller shown in Figure 16. This is a completely different matter for the pressure fluctuation: the pressure change C_p observed in the viscous flow domain Λ is much smaller than predicted by the RANS method with geometrically re-

solved propeller. This difference can be traced back to the fact that in the vicinity of the propeller displacement effects due to the finite blade thickness and chord length become important (A2). However, the virtual propeller emulated by a distribution of body forces is not able to render those effects in the way a geometrically resolved model of the propeller would do this.

Rudder \rightarrow propeller. Regarding the relative change of propeller thrust k_T due to the presence of the rudder given in Figure 9, some discrepancies between the results obtained by the RANS method and the coupling approach can be observed. Although both methods forecast the same tendency,

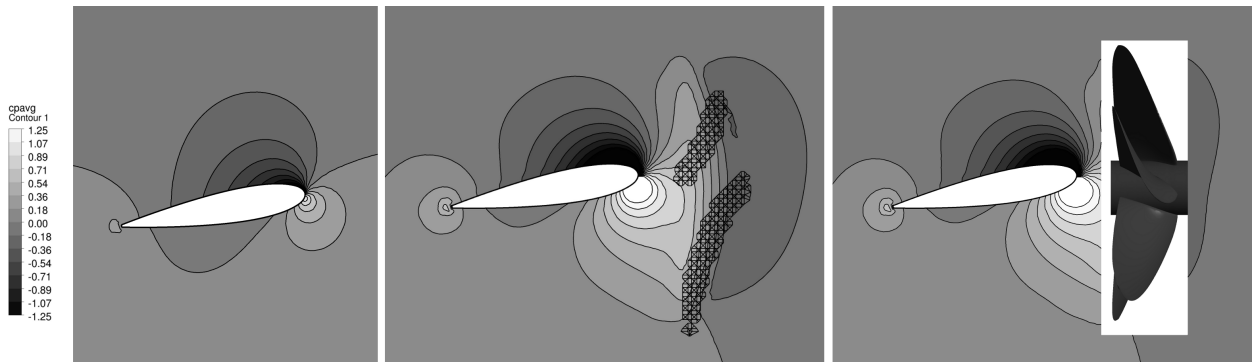


Figure 15: Time-averaged pressure distribution C_p for $z = z_P - 0.5R$ for $J = 0.7$ and $\delta = 10^\circ$. Left: Rudder without propeller, middle: CPL, right: RANS.

the results differ in detail. Whereas the relative increase of thrust predicted by the coupling approach is nearly independent of the advance coefficient J , the increase predicted by the RANS method is higher for $J = 0.7$ than for $J = 0.5$. As explained in Section 3, the blockage effect (B1) of the rudder is captured by incorporating the rudder in the potential flow domain. On the contrary, because of the simplifications made with respect to modelling the propeller slipstream in the potential flow domain, the effect of the reduced slipstream twist on the propeller forces (B2) is not captured. Whereas the former is nearly independent of the propeller load, the latter depends. The same explanation holds for the predicted propeller torque k_Q and for the efficiency η which results from both aforementioned quantities.

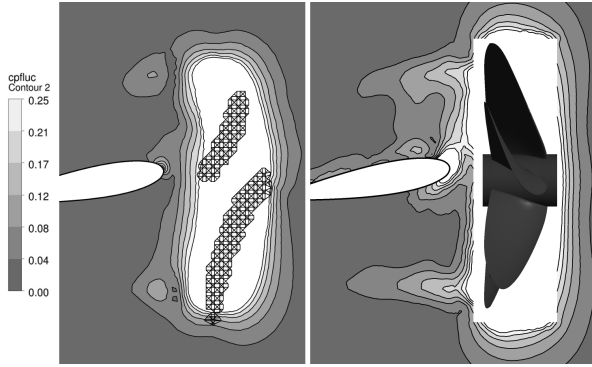


Figure 16: Maximum pressure change C_p for $z = z_P - 0.5R$ for $J = 0.7$ and $\delta = 10^\circ$. Left: CPL, right: RANS.

Despite these somewhat disappointing results for the integral time-averaged propeller forces, the influence of the rudder on the temporal fluctuations of the forces acting on a single blade is captured excellently. For $J = 0.7$ and $\delta = 10^\circ$, the peak value predicted by the coupling approach seems to be overestimated, which may be related to the prescribed propeller wake model.

For non-cavitating flow, the strength of propeller-induced pressure fluctuations depends predominantly on the propeller load and the radial thrust distribution of the propeller blades (Huse 1972). With decreasing distance to the propeller, displacement effects become important. The results in Figure 13 reveal that the simulation tool is able to predict all these effects in a satisfactory manner. Note that the pressure fluctuations have to be observed in the potential flow domain Ω , because, as already stated, the blade displacement cannot be rendered sufficiently by the body force distribution in the viscous flow domain.

4.4 Remarks to the Computational Effort

A converged solution with respect to time-averaged rudder and propeller forces is indispensable for a reliable hydrodynamic analysis of a propeller-rudder combination. For the given configuration, depending on the operation point, converged time-averaged forces are reached after approximately 1.8...2.0 propeller revolutions. Using 32 cores each with 2.6GHz, the developed method needs about 2.5h for the simulation of 7 propeller revolutions.

Table 3: Relative CPU seconds required for the simulation of one revolution.

	RANS	CPL	w/o prop.
CPU time/ rev.	100%	60%	37%

Table 3 helps to estimate the amount of time which can be saved using this method. The RANS solver runs through 3...5 inner iterations per time step, independent of the way the propeller is modelled.

CONCLUSIONS

A simulation tool based on coupling a RANS solver and a panel method has been presented which is able to capture relevant interaction effects between rudder and propeller. Regarding the rudder flow, the method is able to provide results of the same level of detail as a RANS simulation carried out with geometrically resolved propeller. As far as the propeller flow is concerned, some inaccuracies occur. However, they originate from the simplifications made and are thus explainable. The method is able to simulate cavitation effects on the rudder, but the present formulation allows only for the investigation of those cases where propeller cavitation plays a minor role.

ACKNOWLEDGEMENTS

All model test results were kindly provided by the Potsdam Model Basin SVA. The authors would like to thank the German Federal Ministry for Economic Affairs and Energy for the financial support within the research projects *KonKav II*, *NoiseLES*, *OptiStopp* and *PerSee*.

NOMENCLATURE

<i>General variables and constants</i>	
$\mathbf{x} = (x, y, z)$	Space variable in global coordinates
$\mathbf{X} = (X, Y, Z)$	\sim in body-fixed coordinates
t	Time variable
g	Gravity constant
ρ	Density of water
p_v	Vapour pressure of water
<i>Variables potential flow domain Ω</i>	
$\mathbf{U}(\mathbf{x}, t)$	Total velocity in global coordinates
$\mathbf{U}_\infty(y, z, t)$	Background flow velocity in \sim
$\mathbf{U}^+(\mathbf{x}, t)$	Induced velocity in \sim
$\mathbf{U}_\infty^\oplus(\mathbf{x}, t)$	Background flow in a multi-body simulation in \sim
Φ	Induced potential
p	Pressure
μ, σ	Dipole strength, source strength
$\mathbf{V}, \mathbf{V}_{\text{mot}}, \mathbf{V}_\infty, \mathbf{V}^+$	Velocities in body-fixed coordinates
\mathbf{X}_0	Collocation point
\mathbf{n}	Normal vector of a surface element
<i>Variables viscous flow domain Λ</i>	
\mathbf{u}	Reynolds-averaged velocity
p	Reynolds-ave. pressure
$\boldsymbol{\tau}$	Reynolds-ave. molecular stress tensor
$\boldsymbol{\tau}_T$	Reynolds stress tensor
\mathbf{f}	Momentum source term
α_m, α_v	Volume fractions: m liquid, v vaporous
$*$	Material property of mixture

<i>Relevant operation point parameters</i>	
$R, D = 2R$	Propeller radius, diameter
n_b	Number of blades
(x_P, y_P, z_P)	Position of the propeller center in global coordinates
V	Inflow velocity
n	Number of revolutions
$J = \frac{V}{nD}$	Advance coefficient
$k_T = \frac{T}{\rho n^2 D^4}$	Time-ave. thrust coefficient
$k_Q = \frac{Q}{\rho n^2 D^5}$	Time-ave. torque coefficient
$\sigma_V = \frac{p_{\text{ref}} - p_v}{\rho/2V^2}$	Cavitation number
p_{ref}	Reference pressure at $z = z_P$
δ	Rudder angle
<i>Auxiliary quantities</i>	
\sim	Time-ave. quantity
$\hat{\sim}$	Fluctuation or amplitude of a quantity

REFERENCES

- ANSYS. ANSYS CFX 15.0 Documentation. Technical report, ANSYS Inc., Canonsburg, USA, 2014.
- F. Bakir, R. Rey, A. G. Gerber, T. Belamri, and B. Hutchinson. Numerical and Experimental Investigations of the Cavitating Behavior of an Inducer. *International Journal of Rotating Machinery*, 10:15–25, 2004.
- M. Bauer and M. Abdel-Maksoud. A Three-Dimensional Panel Method for the Simulation of Sheet Cavitation in Marine Propeller Flows. In *Proceedings of 83rd Annual Meeting of the Int. Association of Applied Mathematics and Mechanics (GAMM)*, Darmstadt, Germany, 2012.
- S. Berger, M. Bauer, M. Druckenbrod, and M. Abdel-Maksoud. Investigation of Scale Effects on Propeller-Induced Pressure Fluctuations by a Viscous/Inviscid Coupling Approach. In *Proceedings of Third International Symposium on Marine Propulsors (smp'13)*, Launceston, Australia, 2013.
- M. Felli, L. Greco, C. Colombo, F. Salvatore, F. Di Felice, and M. Soave. Experimental and theoretical investigations of propeller-rudder interaction phenomena. In *Proceedings of 26th Symposium on Naval Hydrodynamics*, Rome, Italy, 2006.
- M. Greve, K. Wöckner-Kluwe, Moustafa Abdel-Maksoud, and Thomas Rung. Viscous-Inviscid Coupling Methods for Advanced Marine Propeller Applications. *International Journal of Rotating Machinery*, 2012.
- J.-M. Han, D.-S. Kong, I.-H. Song, and C.-S. Lee. Analysis of the Cavitating Flow around the Horn-type Rudder in the Race of a Propeller. In *Proceedings of Fourth International Symposium on Cavitation (CAV2001)*, Pasadena, USA, 2001.
- E. Huse. Pressure Fluctuations on the Hull Induced by Cavitating Propellers. Technical Report 111, Norwegian Ship Model Experiment Tank, 1972.
- J. Katz and A. Plotkin. *Low-Speed Aerodynamics*. Cambridge University Press, Cambridge, UK, 2nd edition, 2001.
- J.-M. Laurens. Unsteady Hydrodynamic Behaviour of a Rudder Operating in the Propeller Slipstream. *Ship Technology Research*, 50:141–148, 2003.
- D.-Q. Li. A non-linear method for the propeller-rudder interaction with the slipstream deformation taken into account. *Comput. Methods Appl. Mech. Engineering*, 130:115–132, 1996.
- O. A. M. El Moctar. *Numerische Berechnung von Strömungskräften beim Manövrieren von Schiffen*. PhD thesis, Technische Universität Hamburg-Harburg, Hamburg, Germany, 2001.
- A. F. Molland and S. R. Turnock. *Marine Rudders and Control Surfaces*. Elsevier Ltd., 1st edition, 2007. ISBN 978-0-75-066944-3.
- S. Natarajan. *Computational Modeling of Rudder Cavitation and Propeller-Rudder Interaction*. PhD thesis, The University of Texas at Austin, Austin, USA, 2003.
- NMRI. KRISO Container Ship (KCS). https://www.nmri.go.jp/institutes/fluid_performance_evaluation/cfd_rd/cfdws05/Detail/KCS/container.html, 1997. [Online; accessed February 2015].
- H. Richter and H.-J. Heinke. Freifahrt- und Kavitationsversuche sowie Druckschwankungsmessungen mit dem Propeller P1356 in homogener Zuströmung. Technical report, SVA Potsdam, Potsdam, Germany, 2006.
- H. Söding. Limits of Potential Theory in Rudder Flow Predictions. In *Proceedings of 22nd Symposium on Naval Hydrodynamics*, Washington D.C., 1999.
- D. Weicker. Die Vortriebswirkung des Schiffsruders im Propellerstrahl. *Schiffbauforschung*, 4, 1965.

DISCUSSION

Question from Dr. Ki-Han Kim In Figure 13, k_p is higher for $J = 0.7$ than for $J = 0.5$, which is counter-intuitive. Lower J means higher loading, which will induce higher k_p than higher J with lower loading.

Author's Closure For the simulations carried out in this study, the inlet velocity V has been kept constant and $J = \frac{V}{nD}$ has been adjusted by a variation of n . In order to make pressure amplitudes dimensionless, $\rho n^2 D^2$ has been used as denominator, which is different for $J = 0.5$ and 0.7 .